

# Theoretical Determination of the Rate Coefficient for the $\text{HO}_2 + \text{HO}_2 \rightarrow \text{H}_2\text{O}_2 + \text{O}_2$ Reaction: Adiabatic Treatment of Anharmonic Torsional Effects

Dingyu D. Y. Zhou,<sup>†,§</sup> Keli Han,<sup>‡</sup> Peiyu Zhang,<sup>‡</sup> Lawrence B. Harding,<sup>§</sup> Michael J. Davis,<sup>§</sup> and Rex T. Skodje<sup>\*,†,‡,§</sup>

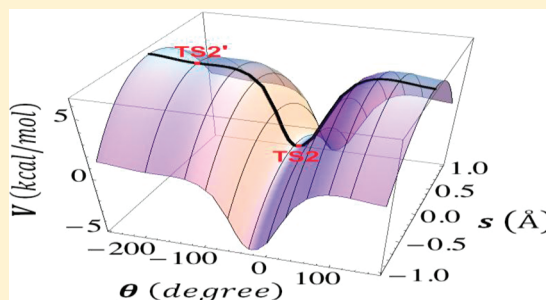
<sup>†</sup>Department of Chemistry and Biochemistry, University of Colorado, Boulder, Colorado 80309-0215, United States

<sup>‡</sup>Key State Laboratory for Reaction Dynamics, Dalian Institute for Chemical Physics, Dalian, China

<sup>§</sup>Chemical Sciences and Engineering Division, Argonne National Laboratory, Argonne, Illinois 60439, United States

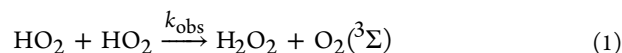
## Supporting Information

**ABSTRACT:** The  $\text{HO}_2 + \text{HO}_2 \rightarrow \text{H}_2\text{O}_2 + \text{O}_2$  chemical reaction is studied using statistical rate theory in conjunction with high level ab initio electronic structure calculations. A new theoretical rate coefficient is generated that is appropriate for both high and low temperature regimes. The transition state region for the ground triplet potential energy surface is characterized using the CASPT2/CBS/aug-cc-pVTZ method with 14 active electrons and 10 active orbitals. The reaction is found to proceed through an intermediate complex bound by approximately 9.79 kcal/mol. There is no potential barrier in the entrance channel, although the free energy barrier was determined using a large Monte Carlo sampling of the  $\text{HO}_2$  orientations. The inner (tight) transition state lies below the entrance threshold. It is found that this inner transition state exhibits two saddle points corresponding to torsional conformations of the complex. A unified treatment based on vibrational adiabatic theory is presented that permits the reaction to occur on an equal footing for any value of the torsional angle. The quantum tunneling is also reformulated based on this new approach. The rate coefficient obtained is in good agreement with low temperature experimental results but is significantly lower than the results of shock tube experiments for high temperatures.



## I. INTRODUCTION

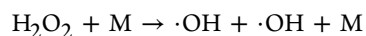
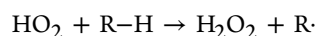
The self-reaction of the hydroperoxy radical,  $\text{HO}_2$ , is an important process in atmospheric and combustion chemistry. As such, it has been repeatedly studied over the last several decades.<sup>1–28</sup> It is believed that this reaction is the primary source for hydrogen peroxide in the stratosphere and is an important participant in atmospheric  $\text{HO}_x$  chemistry. For high temperature combustion problems, the  $\text{HO}_2$  self-reaction plays a critical role in the ignition process. It is believed that the primary product channel for self-reaction is the triplet process



which is highly exothermic,  $\Delta H_{\text{rxn}}(298 \text{ K}) = -38.2 \text{ kcal/mol}$ .<sup>29</sup> In addition to reaction 1, several minor channels have been observed (or conjectured) that yield the  $\text{H}_2 + 2\text{O}_2(^3\Sigma)$ ,  $\text{H}_2\text{O}_2 + \text{O}_2(^1\Delta)$ , or  $\text{H}_2\text{O} + \text{O}_3$  products.<sup>13,30</sup>

We are motivated to reconsider the  $\text{HO}_2 + \text{HO}_2$  reaction kinetics at this time by our recent investigation of the global sensitivity analysis of autoignition delay times for various combustion fuels.<sup>31–33</sup> Our goal in that work was to systematically improve theoretical combustion mechanisms by using high level ab initio quantum chemistry and transition state theory (TST) to compute more accurate rate coefficients.

We targeted for re-evaluation those rate coefficients in the mechanism that are simultaneously highly sensitive and highly uncertain. Therefore, there is a good likelihood that a more precise determination of these rate coefficients would reduce the overall uncertainty of important predictions of the mechanism. For the autoignition of methanol, butanol, and hydrogen, it was found that the global sensitivity coefficient for the  $\text{HO}_2 + \text{HO}_2$  reaction was consistently among the largest. The  $\text{HO}_2$  radical plays an important role in the ignition process through the reaction sequence<sup>34</sup>



Thus, in this cycle, one  $\text{HO}_2$  radical generates three radicals which greatly contribute to the chain branching. Reaction 1 proves to be a sensitive reaction since it inhibits this sub-mechanism. One of our primary objectives in the present work is to update the rate coefficient for the self-reaction of  $\text{HO}_2$  at combustion temperatures. Since there does not currently exist a

Received: October 8, 2011

Revised: January 24, 2012

Published: February 3, 2012



high level computation of the rate coefficient, it appears to be a good candidate for study.

On a fundamental level, reaction 1 exhibits several interesting characteristics that have attracted attention. First, the temperature dependence of the observed  $k_{\text{obs}}(T)$  reveals a clear minimum near  $T = 700\text{--}800$  K, as the activation energy shifts from negative at low temperature to positive at high temperature. Second, the rate exhibits a substantial pressure dependence at low  $T$  which apparently disappears above about  $T = 600$  K. Finally, there appears to be a strong dependence of the reaction rate on the concentration of gas phase water<sup>45</sup> and methanol<sup>23</sup> at low  $T$ . The influence of water is a serious matter since substantial amounts of  $\text{H}_2\text{O}$  are almost always present in laboratory measurements. The  $\text{HO}_2 + \text{HO}_2$  reaction was one of the earliest examples of water catalysis of gas phase water reactions.

A relatively straightforward mechanism has emerged to account for these observations based on the presumed existence of an intermediate complex,  $\text{H}_2\text{O}_4$ . Mozurkewich and Benson<sup>12</sup> suggested that the energetic profile along the reaction coordinate should resemble the schematic shown in Figure 1.

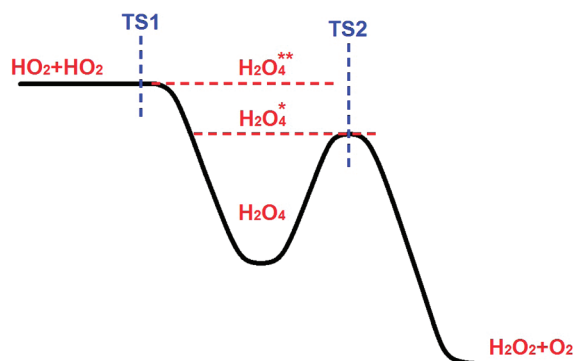
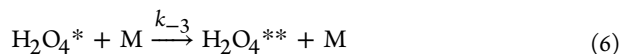
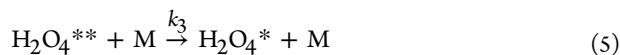
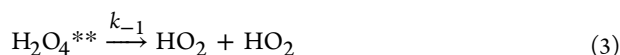


**Figure 1.** Schematic diagram showing the two bottleneck model of the  $\text{HO}_2 + \text{HO}_2$  reaction. The reaction is barrierless, so TS1 is a loose transition state. The tight transition state is submerged (i.e., lower than the entrance channel). The “species”  $\text{H}_2\text{O}_4^{**}$  and  $\text{H}_2\text{O}_4^*$  are accessible only by third body collision.

Thus, in the presence of a buffer gas (M), the reaction is described by the multistep mechanism



The distinction between the “species”  $\text{H}_2\text{O}_4^{**}$ ,  $\text{H}_2\text{O}_4^*$ , and  $\text{H}_2\text{O}_4$  is based on the energetics of Figure 1. While the observation of a negative activation energy was generally ascribed<sup>35,36</sup> to barrierless complex formation, various aspects of this mechanism remained unclear. The structure of the intermediate was

undetermined during the earliest investigations. Giguere and Herman,<sup>37</sup> e.g., identified a linear chain “tetraoxy” structure,  $\text{HOOOOH}$ , for the intermediate in matrix isolation studies. Patrick et al.<sup>8</sup> and Kircher et al.<sup>10</sup> carried out modeling studies of the  $\text{HO}_2$  self-reaction using the tetraoxide form. Alternatively, a doubly hydrogen-bonded ring structure was also proposed<sup>38,39</sup> that was used by Mozurkewich and Benson. Recent quantum chemistry calculations have now clearly established that the latter hydrogen-bonded structure was in fact the most stable form of the gas phase intermediate.<sup>19,25</sup> Likewise, the precise nature of the transition state was also the subject of some debate.

The pressure dependence of the reaction reflects the influence of the collisions of the background gas M with the intermediate,  $\text{H}_2\text{O}_4$ . As the pressure of M goes up, the overall rate increases since the back reaction, eq 3, is partially suppressed by the collisional energy transfer processes through process 5. The sensitivity of the reaction to water was explained by the assumed formation of the  $\text{HO}_2 \cdot \text{H}_2\text{O}$  complex. The observations are explained if this complex is presumed to be more reactive with  $\text{HO}_2$  than is  $\text{HO}_2$  in the uncomplexed form.

At present, there is no first principles calculation of the  $\text{HO}_2 + \text{HO}_2$  rate coefficient. The early theoretical treatments of Mozurkewich and Benson<sup>12</sup> and of Patrick et al.,<sup>8</sup> while physically well grounded, rely heavily on the use of empirical parameters. As such, these treatments do not provide an independent check on possible experimental error. One impediment to an accurate RRKM calculation has been the difficulty in obtaining reliable electronic structure results. Single reference calculations are not adequate for this system, and it is necessary to carry out much more demanding CASPT2 or MRCI treatments of this problem. It is also necessary to include the effects of quantum tunneling since the reaction coordinate is largely H-atom motion and the imaginary frequency at the barrier turns out to be quite large. The most challenging aspect of this reaction is the role of lowest frequency torsional motion in the transition state complex. As noted above, the intermediate is a doubly hydrogen-bonded ring structure. The transition state is found to multifaceted. That is, there are two distinct saddle points associated with two conformations of a torsional coordinate of the  $\text{H}_2\text{O}_4$  adduct. In this work we present a new unified treatment of the multifaceted transition state based on the vibrationally adiabatic model.

The remainder of this paper is organized as follows. The general structure of the rate coefficient is presented in section II. Working in a microcanonical representation, our derivation closely follows that of Murukewich and Benson<sup>38</sup> and Chen et al.<sup>39</sup> and provides a first principles representation of the rate coefficient. The influence of pressure is included using a master equation formalism. In section III, we discuss the electronic structure calculations carried out for the  $\text{HO}_2 + \text{HO}_2$  reaction. In section IV we present the procedures used for the numerical calculation of the rate coefficient. The highlight of this section is the adiabatic treatment of the torsional motion that permits a unified treatment of the multiple transition states. In section V the methods used for quantum tunneling are presented. It is found that the unified treatment of the multifaceted transition state also requires a new formulation of the quantum tunneling. In section VI the final form of the new rate coefficient is presented and discussed. While the rate coefficient obtained agrees well with low temperature experiments, it is lower than experiment in the high temperature regime.

## II. THE FORM OF THE RATE COEFFICIENT

The statistical rate theory for a reaction that proceeds through an intermediate complex, C, viz.,  $A + B \leftrightarrow C \rightarrow P$ , has been formulated previously by Mozurkewich et al.<sup>40</sup> and Chen et al.<sup>41</sup> and has been discussed by Georgievskii and Klippenstein.<sup>42</sup> Here, we shall briefly review and adapt this treatment. Using a notation consistent with Figure 1, the outer transition state, TS1, is loose and is characterized by the cumulative density of states  $N_1^\ddagger(E, J)$ . The energy zero lies at the ground state in the reagent channel.  $J$  is the magnitude of the total angular momentum. The inner transition state, TS2, is tight and has the cumulative density of states  $N_2^\ddagger(E, J)$ . The zero-point corrected barrier lies at the negative value  $E_{TS2}^\ddagger < 0$ . Since the energy zero remains set at the entrance channel threshold,  $N_2^\ddagger(E, J)$  will be nonzero for the negative energies  $E_{TS2}^\ddagger < E < 0$ . However, in the absence of third body collisions these energies are inaccessible. Using RRKM theory for fixed  $E$  and  $J$ , the microcanonical rate coefficient for the complex going forward to products is the following, where  $C = H_2O_4$

$$k_2(E, J) = \frac{N_2^\ddagger(E, J)}{h\rho_C(E, J)} \quad (2.1)$$

while the rate coefficient for going backward to reagents is

$$k_{-1}(E, J) = \frac{N_1^\ddagger(E, J)}{h\rho_C(E, J)} \quad (2.2)$$

We use  $\rho_C(E, J)$  for the state density of the intermediate  $H_2O_4$  at fixed  $E$  and  $J$ .

Collisions between the intermediate and the background gas lead to energy and angular momentum transfer that may affect the rate. In the “high pressure limit”, many such collisions occur and the first-order decay rate coefficients  $k_{-1}$  and  $k_2$  are given by canonical TST expressions. Conversely, in the low pressure regime, the complex is formed and decays without additional collisions and, thus,  $E$  and  $J$  are conserved in microcanonical ( $\mu C$ ) representation. Since the  $H_2O_4$  complex is not strongly bound and the lifetimes are short, we expect the collision free  $\mu C$  form should be accurate at elevated temperatures, which will be derived explicitly. The effect of collisions over a wide range of pressures and temperatures shall quantitatively modeled using a master equation approach with empirically chosen parameters.

In the collision free limit, the reaction can be described by a complex formation step followed by a decay step. The rates of formation and decay of the complex are governed by transition state bottlenecks, TS1 and TS2, at the same  $(E, J)$  since these variables are conserved. Assuming statistical branching, once formed the complex will decay into the entrance and exit channels with a branching ratio of

$$\beta(E, J) = \frac{k_2(E, J)}{k_{-1}(E, J)} = \frac{N_2^\ddagger(E, J)}{N_1^\ddagger(E, J)} \quad (2.3)$$

The rate of product formation is obtained using a steady state approximation for the intermediate and is given by

$$\begin{aligned} \frac{d[P]}{dt} &= \int_0^\infty dJ \int_0^\infty dE e^{-E/k_B T} k_2(E, J) [C(E, J)]_{ss} \\ &= k_{obs}(T) [A][B] \end{aligned} \quad (2.4)$$

where we have made the continuum approximation for the angular momentum. Inserting the steady state expression for the concentration  $[C(E, J)]_{ss}$  we find

$$\begin{aligned} k_{obs}(T) &= \frac{1}{hQ_A Q_B} \int_0^\infty dJ \int_0^\infty dE e^{-E/k_B T} \\ &\times \frac{N_1^\ddagger(E, J) N_2^\ddagger(E, J)}{N_1^\ddagger(E, J) + N_2^\ddagger(E, J)} \end{aligned} \quad (2.5)$$

where  $Q_A$  and  $Q_B$  are the canonical partition functions per unit volume for the reagents. Equation 2.5 provides the general expression that we shall employ for the low-pressure rate coefficient for the  $HO_2$  self-reaction. It important to note that the effective bimolecular rate coefficient eq 2.5 does not depend on the detailed properties of the complex since the density of states  $\rho_C(E, J)$  has canceled out in the final expression. Instead, the rate depends on the two bottlenecks, TS1 and TS2, through the ratio  $N_1^\ddagger(E, J) N_2^\ddagger(E, J) / (N_1^\ddagger(E, J) + N_2^\ddagger(E, J))$ .

To estimate the pressure dependence of  $k_{obs}(T)$  due to collisions with a background gas (here assumed to be  $N_2$ ), we employ a conventional master equation formulation.<sup>43,44</sup> In contrast to the first principles calculation described above for the low pressure limit, this approach is empirical in that the Lennard-Jones parameters,  $(\epsilon, \sigma)$ , and energy transfer probabilities,  $P(E, E')$ , must be fit to experimental data. The concentration density of the intermediate at energy  $E$  and time  $t$  (summed over all  $J$ ) is given by  $X(E, t)$ . The rate of collisional energy transfer ( $E \rightarrow E'$ ) of the intermediate is described by the rate kernel

$$k(E, E') = \omega \cdot P(E, E') \quad (2.6)$$

where collision frequency is

$$\omega = \mathbb{N} \cdot \pi \sigma^2 \cdot \Omega \cdot \sqrt{\frac{8k_B T}{\pi \mu}} \quad (2.7)$$

where  $\mathbb{N}$  is the buffer gas concentration,  $\mu$  the reduced mass of  $N_2$  with  $H_2O_4$ , and

$$\Omega = \frac{1}{0.636 + 0.246 \cdot \ln\left(\frac{k_B T}{\epsilon}\right)} \quad (2.8)$$

The energy transfer probability function is taken to be the exponential “down” form

$$P(E, E') = \frac{\exp\left[\frac{-(E - E')}{\alpha}\right]}{M(E)} \quad E > E' \quad (2.9)$$

where  $M(E)$  is the normalization constant and the “up” transition probability, for  $E' > E$ , is set by microreversibility. The collisions between  $N_2$  and  $H_2O_4$  are modeled using  $\alpha = 1.88$  kJ/mol (a value used previously by Patrick et al.<sup>9</sup>),  $\sigma = 6$  Å, and  $\epsilon = 1200$  K. The rate of change of the concentration density is given by the kinetic equation

$$\begin{aligned} \frac{dX(E, t)}{dt} &= S(E) + \int_{Emin}^{+\infty} k(E', E) \cdot X(E', t) \cdot dE' \\ &\quad - \int_{Emin}^{+\infty} k(E, E') \cdot X(E, t) \cdot dE' \\ &\quad - k_{-1}(E) \cdot X(E, t) - k_{-2}(E) \cdot X(E, t) \end{aligned} \quad (2.10)$$

Table 1

	zero-point-corrected energies (kcal/mol)				
	reagents (HO <sub>2</sub> + HO <sub>2</sub> )	intermediate (H <sub>2</sub> O <sub>4</sub> )	TS2	TS2'	products (H <sub>2</sub> O <sub>2</sub> + O <sub>2</sub> )
present result <sup>a</sup>	0.00	−9.79	−4.22	0.45	−38.15 <sup>d</sup>
CASPT2/6-311+G(3df,2p) <sup>b</sup>	0.00	−8.80	−3.00	−1.10	−39.50
B3LYP/6-311G(d,p) <sup>c</sup>	0.00	−11.80	−8.10	−5.50	−33.80
MP2/6-311G(d,p) <sup>c</sup>	0.00	−8.60	2.00	2.50	−51.70
MP2/6-311+G(3df,2p) <sup>c</sup>	0.00	−8.50	1.80	2.60	−51.40
CCSD(T)/6-311G(d,p) <sup>c</sup>	0.00	−9.60	−0.36	1.60	−38.50
G2M <sup>c</sup>	0.00	−9.50	−0.50	1.70	−38.20
	imaginary frequency (cm <sup>−1</sup> )				
			TS2	TS2'	
present result <sup>a</sup>			2548.6i	3466.7i	
CASSCF/6-311+G(3df,2p) <sup>b</sup>			4709.2i	4896.7i	
	T1 diagnostic value				
	reagents (HO <sub>2</sub> + HO <sub>2</sub> )	intermediate (H <sub>2</sub> O <sub>4</sub> )	TS2	product (H <sub>2</sub> O <sub>2</sub> )	product (O <sub>2</sub> )
CCSD(T)/cc-pVDZ <sup>e</sup>	0.0362	0.0423	0.0545	0.00992	0.00604

<sup>a</sup>The geometry and frequencies of the reactants (two HO<sub>2</sub> radicals separated by 10 Å) and the intermediate (H<sub>2</sub>O<sub>4</sub>). TS2 and TS2' are calculated by the method CASPT2/aug-cc-pVTZ with 6 active electrons and 6 active orbitals (2σ<sub>OH</sub>, 2σ\*<sub>OH</sub>, and 2π\*<sub>OO</sub>), but their energy is calculated using CASPT2/aug-cc-pVTZ/CBS with 14 active electrons and 10 active orbitals (2σ<sub>OH</sub>, 2σ\*<sub>OH</sub>, 4π<sub>OO</sub>, and 2π\*<sub>OO</sub>). <sup>b</sup>Reference 25. <sup>c</sup>Reference 19. <sup>d</sup>The product state calculations did not require a multireference treatment and were obtained using CCSD(T)/aug-cc-pVTZ/CBS. The result is close to the experimental value of −38.3 kcal/mol. <sup>e</sup>The geometry and energy for all species are calculated using CCSD(T)/cc-pVDZ.

where  $E_{\min}$  is the (negative) zero point of the intermediate. The chemical source term,  $S(E)$ , describes complex formation from  $A + B$  (i.e., HO<sub>2</sub> + HO<sub>2</sub>)

$$S(E) = \frac{N_1^\ddagger(E) \cdot e^{-E/k_B T}}{h \cdot Q_A Q_B} \cdot [A][B] \quad (2.11)$$

The decay of the complex to reagents and products is governed by the rate coefficients

$$k_{-1}(E) = \frac{N_1^\ddagger(E)}{h \cdot \rho_C(E)} \quad (2.12)$$

and

$$k_2(E) = \frac{N_2^\ddagger(E)}{h \cdot \rho_C(E)} \quad (2.13)$$

The details of the  $J$ -summing and other computational procedures are discussed in section IV. The overall pressure dependent rate coefficient is formally given by the expression

$$k_{\text{obs}}(T, p) = \frac{\int_{E_{\min}}^{+\infty} k_2(E) \cdot X(E) \cdot dE}{[A][B]} \quad (2.14)$$

In eq 2.14,  $X(E)$  is computed for steady state where  $dX(E, t)/dt = 0$  in eq 2.10. It is easily verified that the concentration dependence of  $k_{\text{obs}}(T, p)$  cancels out.

### III. QUANTUM CHEMISTRY

As noted in the Introduction, there have been numerous electronic structure calculations performed on the HO<sub>2</sub> + HO<sub>2</sub> system that have yielded a wide range of results.<sup>19,20,25,45,46</sup> Most of the early attempts involved single reference calculations for the stationary points of the potential, most importantly the intermediate and TS2. The results of Lin and co-workers<sup>19</sup> at the CCSD(T)/6-311G(d,p) and G2M levels confirmed that the most stable triplet intermediate was a doubly hydrogen-bonded

six member ring, see Table 1. Relative to reagents, the intermediate was stabilized by 9.6 or 9.5 kcal/mol for the two methods, respectively. For both methods, the lowest transition state to H<sub>2</sub>O<sub>2</sub> + O<sub>2</sub> products was “submerged”, i.e., lying below the entrance channel threshold. Several additional stationary points were located that correspond to the double H-atom exchange process and to further conformational structures.

Since the HO<sub>2</sub> + HO<sub>2</sub> system involves four oxygen atoms with two unpaired electrons, one expects that the multireference character of the wave function may affect the results. Indeed, our computation of the T1 diagnostic for multireference character at the TS2 structure yielded a result of 0.055, far higher than the <0.02 value generally accepted for the validity of single reference calculations. Anglada et al.<sup>25</sup> have recently carried out calculations using multireference complete active space (CAS) methods which did yield results quite different from Lin's single reference calculations. They optimized geometry and calculated frequencies using the CASSCF/6-311+G(3df,2p) method with a small active space of 8 active orbitals and 10 active electrons, i.e., (8o, 10e), for the intermediate and (9o, 11e) for the transition state. They then calculated the energy using the perturbation method<sup>47</sup> CASPT2/6-311+G(3df,2p) method with a larger active space (12o, 14e). A potential problem is that the use of the CASSCF method to optimize the geometries may yield error in the barrier energies and frequencies. Indeed, Anglada et al. report an imaginary frequency of 4709i cm<sup>−1</sup> for TS2 implying that even a small error in geometry may lead to a large error in the energy of the transition state, although the energy calculation is done at a higher level.

To reduce the error incurred in the geometry optimization, we have undertaken a new set of CAS calculations using the MOLPRO 2010 package.<sup>48</sup> The geometries and frequencies are now computed using CASPT2 which we expect to yield higher accuracy than the previous results using CASSCF. The energies of the reagents, intermediate, and transition states were carried out using the same basis set and quantum method for consistency. The geometry optimization and frequencies were obtained using CASPT2/aug-cc-pVTZ with 6 active electrons



and 6 active orbitals (6o, 6e) ( $\sigma_{\text{O}_2\text{H}_5}$ ,  $\sigma^*_{\text{O}_2\text{H}_5}$ ,  $\sigma_{\text{O}_4\text{H}_6}$ ,  $\sigma^*_{\text{O}_4\text{H}_6}$ ,  $\pi^*_{\text{O}_1\text{O}_2}$ , and  $\pi^*_{\text{O}_3\text{O}_4}$ ). The reagent optimization was carried at a center of mass separation between the  $\text{HO}_2$  radicals of 10 Å. The energies were obtained from single point calculations using CASPT2/aug-cc-pVTZ with 14 active electrons and 10 active orbitals (10o, 14e) ( $\sigma_{\text{O}_2\text{H}_5}$ ,  $\sigma^*_{\text{O}_2\text{H}_5}$ ,  $\sigma_{\text{O}_4\text{H}_6}$ ,  $\sigma^*_{\text{O}_4\text{H}_6}$ ,  $\pi_{\text{O}_1\text{O}_2}$ ,  $\pi_{\text{O}_1\text{O}_2}$ ,  $\pi_{\text{O}_3\text{O}_4}$ ,  $\pi_{\text{O}_3\text{O}_4}$ ,  $\pi^*_{\text{O}_1\text{O}_2}$ , and  $\pi^*_{\text{O}_3\text{O}_4}$ ). More accurate energies are then obtained by an extrapolation to the complete basis set (CBS) limit<sup>49</sup> using the CASPT2 calculations with the aug-cc-pVDZ, aug-cc-pVTZ, and aug-cc-pVQZ basis sets. For completeness, we also undertook the computation of the product channel properties, although this is not required for the determination of the rate coefficient. It was difficult to optimize the orbitals for the product channel in a manner consistent with the transition state and reagents. However, since the T1 diagnostic value for the product species is small, a single reference method was chosen instead which obviates the need to construct the active space. The product energy, geometry, and frequencies were obtained using CCSD(T)/CBS/aug-cc-pVTZ.<sup>50</sup> The zero-point-corrected energy of reaction obtained in this way was  $\Delta E_0 = -38.15$  kcal/mol. We note in passing that the product state energy obtained using CCSD(T) is over 6 kcal/mol higher than the corresponding CASPT2 result with (10o, 14e), which clearly illustrates the difficulty in selecting the correct active space. If a full valence calculation of the reagents and products is carried out (which was not feasible for the transition state), we obtain a CASPT2/CBS result of  $\Delta E_0 = -38.76$  kcal/mol in agreement with the CCSD(T) method.

Since the T1 diagnostic is 0.036 for the  $\text{HO}_2$  radical itself, it appears also necessary to use multireference methods to characterize the loose transition state in the entrance channel, TS1. The objective of these computations is not to find stationary points but rather to sample the relative orientations of the two  $\text{HO}_2$  asymmetric tops as a function of the intermolecular separation. Since on the order of  $10^5$  computations are required, a more efficient method was employed, viz., CASPT2/aug-cc-pVDZ with (2o, 2e), i.e., two  $\pi^*$  orbitals for two unpaired electrons. The results of this (2o, 2e) calculation used for the computation of  $N^\ddagger(E, J)$  at TS1 is shifted to be consistent with the (10o, 14e) calculation presented in Table 1.

The optimized structures obtained are shown in Figure 2, while the energetics is presented in Table 1. The normal-mode frequencies are presented in Table 2. The characteristics of the intermediate and transition states we obtained are qualitatively similar to those of Anglada et al.,<sup>25</sup> although there are quantitative differences. In our calculations, the doubly hydrogen-bonded intermediate is more strongly bound by about 1.0 kcal/mol while the TS2 barrier is further submerged by about 1.2 kcal/mol. However, the most important differences between the two sets of calculations lie with the geometries. For example, the O2–H5–O3 bond lengths for the H-atom transfer at the TS2 structure were found to be  $R_{2,5} = 1.131$  Å and  $R_{3,5} = 1.266$  Å in our computations while they were found to be  $R_{2,5} = 1.175$  Å and  $R_{3,5} = 1.211$  Å by Anglada et al. The O1–O2 bond length at TS2 was  $R_{1,2} = 1.256$  Å in our calculation and was  $R_{1,2} = 1.293$  Å in that of Anglada et al. The optimization of the torsional conformer of the transition state, TS2' (see below), is even more different. We obtained  $R_{2,5} = 1.109$  Å and  $R_{3,5} = 1.277$  Å, while they obtained  $R_{2,5} = 1.171$  Å and  $R_{3,5} = 1.214$  Å. In addition to the large geometry differences between the CASSCF and CASPT2 optimized geometries, we also find the vibrational frequencies were also quite different. As shown in Table 1, the imaginary barrier frequency is seen to

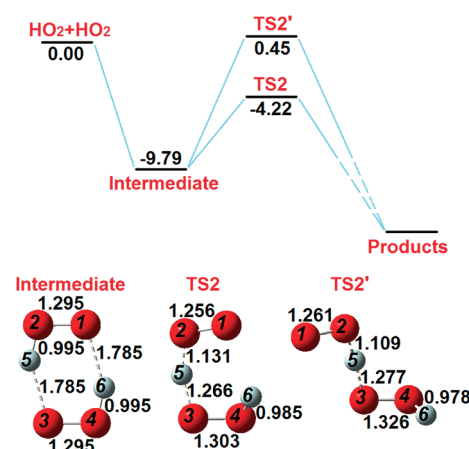


**Figure 2.** Energies and structures of the stationary points on the ground triplet potential energy surface obtained using CASPT2/aug-cc-pVTZ (6o, 6e) for geometries and CASPT2/CBS/aug-cc-pVTZ (10o, 14e) for the energies. The distances are in Å and the harmonic zero-point-corrected energies are in kcal/mol.

**Table 2**

	normal-mode frequencies of stationary points ( $\text{cm}^{-1}$ ) <sup>a</sup>
$\text{HO}_2$	3600.8, 1451.7, 1217.4
intermediate	3355.7, 3263.1, 1577.6, 1560.1, 1315.6, 1310.5, 749.7, 612.0, 296.9, 264.5, 206.3, 109.9
TS2	3500.7, 1774.7, 1531.2, 1485.9, 1313.3, 1125.7, 691.6, 426.4, 356.5, 209.5, 119.7, 2548.6i
TS2'	3598.0, 1603.0, 1461.0, 1438.7, 1222.0, 842.2, 657.2, 407.0, 263.8, 100.5, 16.7, 3466.7i

<sup>a</sup>See footnote a of Table 1

differ by almost a factor of 2. Despite the high level of the present calculation, we still expect errors on the order of 1 kcal/mol due to the use of perturbation theory and limitations of the basis set and active space.

We need to also be cognizant of the electronic degeneracies when computing the partition functions. The  $\text{HO}_2$  species forms an electronic doublet; thus, the  $\text{HO}_2 + \text{HO}_2$  asymptote will consist of four degenerate levels, a triplet, and a singlet. The reaction is assumed to occur only on the triplet surfaces which correlate with the ground state products. Thus, we shall multiply the nuclear rate coefficient by a temperature independent multisurface factor of 3/4.

Finally, it is important to highlight the role of the torsional motion at the transition state. The lowest frequency (i.e.,  $119.7 \text{ cm}^{-1}$ ) normal mode of TS2 is found to correspond nicely with a torsional motion involving the four oxygen atoms. Specifically, the dihedral angle is formed from the  $\text{R}(\text{O1}–\text{O2})$  and  $\text{R}(\text{O3}–\text{O4})$  vectors with the  $\text{R}(\text{O2}–\text{O3})$  axis. Interestingly, the second transition state, TS2', is found at a torsional displacement of  $142.1^\circ$  from TS2 with the remaining bond lengths and bond angles only changing modestly. The optimized structures as a function of the torsional coordinate are shown in Figure 3. The energy of TS2' is 4.67 kcal/mol higher than TS2. It is important to note that the normal-mode frequencies are also quite different, as seen in Table 2. The torsion at TS2' now exhibits a frequency of merely  $16.7 \text{ cm}^{-1}$ , suggesting it likely behaves as a free rotor. The next lowest modes have frequencies ( $356.5 \text{ cm}^{-1}$ ,  $209.5 \text{ cm}^{-1}$ ) for TS2, while for TS2' they are ( $263.8 \text{ cm}^{-1}$ ,  $100.5 \text{ cm}^{-1}$ ). We shall show that both transition states need be included in the rate

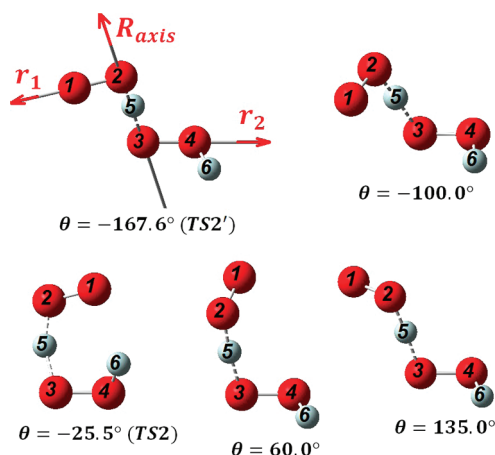


**Figure 3.** Configurations of the  $\text{H}_2\text{O}_4$  adduct as a function of the dihedral angle for the low frequency torsional mode.

coefficient calculation. The other torsional motions in the  $\text{H}_2\text{O}_4$  complex are less important and will be treated using the normal mode model. We note, however, that there exists a mirror image configuration for both TS2 and TS2' that requires an overall factor of 2 for  $N_2^\ddagger(E, J)$ .

#### IV. NUMERICAL DETERMINATION OF THE STATE DENSITIES INCLUDING TORSION ANHARMONICITY

The determination of the rate coefficient requires the numerical evaluation of the state densities  $N_1^\ddagger(E, J)$  and  $N_2^\ddagger(E, J)$  using the data obtained from the ab initio calculations. For the most part, these calculations employed standard methods that were implemented using subroutines adapted from the Polyrate<sup>51</sup> and VariFlex<sup>52</sup> software packages. Here, we shall give only very brief reviews of those known methods. The main emphasis of this section is the treatment of torsional nonseparability for TS2 and TS2'.

**A. The Loose Transition State: TS1.** The association reaction  $\text{HO}_2 + \text{HO}_2 \xrightarrow{k_1} \text{H}_2\text{O}_4$  is a barrierless process described by a loose transition state. We calculate  $N_1^\ddagger(E, J)$ , the total ro-vibration cumulative state density for fixed  $E$  and  $J$ , using the variable reaction coordinate transition state method (VRC-TST).<sup>53</sup> The VRC-TST calculations are performed by using the Polyrate 2010A package along with our own interface between Polyrate and Molpro. In these computations, the distance between the centers of mass of the rigid  $\text{HO}_2$  radicals is held fixed and the CASPT2/aug-cc-pVDZ energy is computed for a Monte Carlo sample of relative orientations. We carry out these calculations for 50 separation distances between 2.5 and 10 Å using MC sample sizes of 2000 orientations. The local minimum of the smoothed density of states curve is used to define the location of the transition state. (This is a small modification of Polyrate which uses the global minimum.) We estimate the MC sampling error for  $N_1^\ddagger(E, J)$  to be approximately 1% or less.

**B. Normal-Mode Treatment of TS2 and TS2'.** It is straightforward to implement the conventional harmonic oscillator–rigid rotor treatment for  $N_2^\ddagger(E, J)$  at TS2. The energy levels of the transition state are obtained from the normal-mode vibrational frequencies computed by CASPT2/aug-cc-pVTZ (60, 6e), the symmetric top approximation for the rotational states, and the saddle point energy from CASPT2/CBS/aug-cc-pVTZ (100, 14e). The state sums are

carried out using the Beyer–Swinehart<sup>54</sup> algorithm for the vibrational levels,  $N_{\text{TS2}}^\ddagger(E)$  and then (up to the overall rotational degeneracy of  $2J + 1$ )

$$N_{\text{TS2}}^\ddagger(E, J) = N_{\text{TS2}}^\ddagger \left( E - \frac{\hbar^2 J(J+1)}{2I_1} \right) + \sum_{k=1}^J 2 \cdot N_{\text{TS2}}^\ddagger \left( E - \left[ \frac{\hbar^2 J(J+1)}{2I_1} + \hbar^2 k^2 \left( \frac{1}{2I_3} - \frac{1}{2I_1} \right) \right] \right) \quad (4.1)$$

where  $I_1$  and  $I_3$  are the moments of inertia computed for the TS2 geometry. The calculation of the cumulative state density for TS2' is carried out in a similar way. The one modification required is that the torsional normal mode is replaced with a free rotor since its frequency is only  $17 \text{ cm}^{-1}$  and the barrier to hindered rotation is  $5 \text{ cm}^{-1}$ .

We also carried out certain calculations with a separable hindered rotor model of the torsional motion. In those computations, the energy levels of the torsional coordinate ( $\theta$ ) motion are obtained by solving the one-dimensional Schrödinger equation using a potential function obtained by relaxing the geometry at each  $\theta$ . The remaining normal modes were treated in the usual harmonic oscillator fashion from TS2 frequencies.

**C. Semiclassical Adiabatic Treatment of the Torsional Motion.** As we have noted above, the torsional motion is problematic in the  $\text{HO}_2 + \text{HO}_2$  reaction. The two configurations, TS2 and TS2', essentially correspond to conformational isomers of the transition state lying at  $\theta = -25.5^\circ$  and  $\theta = -167.6^\circ$ , where  $\theta$  is the dihedral angle. While there are two other modes that might also be regarded as torsional, we did not find additional saddle points for those degrees of freedom (aside from the mirror image configurations). Multifaceted transition states have received some attention in the recent literature<sup>55,56</sup> and are expected to be generic for systems with energetically accessible torsional conformers. Truhlar and co-workers<sup>57</sup> have suggested the MS-AS method in which the contributions for the various transition state structures are summed using several possible weighting factors. The  $\text{HO}_2 + \text{HO}_2$  reaction is a particularly challenging case since remaining vibrational modes are strongly coupled to the torsion as is clear from the large variation in the frequencies seen in Table 2. Furthermore, since the barrier to hindered rotation for TS2' is very low,  $5 \text{ cm}^{-1}$ , it is not meaningful to compute the state sums using local potential expansions around TS2'. On the other hand, the usual separable hindered rotor approximation for the remaining modes is questionable because of the strong anharmonicity and mode coupling.

We present a unified approach for a single torsional coordinate in which the reaction can proceed across the barrier for any value of the dihedral angle and is not restricted to occur near the stationary points TS2 or TS2'. As illustrated in Figure 4, TS2 and TS2' correspond to two points on a transition state ridge, and it is clear that for sufficiently high energy the system may cross the ridge at any value of  $\theta$ . Unlike a saddle point which is a single geometry, the ridge is a one-dimensional curve in the configuration space of the complex that we can parametrize with the dihedral angle, i.e.,  $\mathbf{R}(\theta)$ . We can compute this ridge curve to high accuracy using the following procedure.

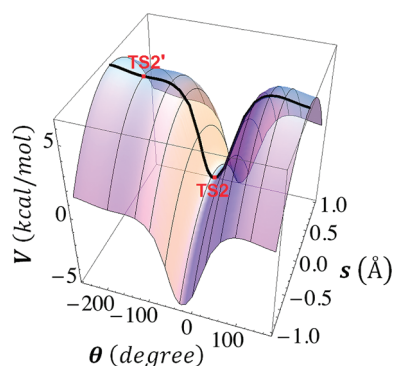


**Figure 4.** Potential energy surface as a function of the reaction coordinate,  $s$ , and the dihedral angle,  $\theta$ . The remaining normal-mode coordinates have been relaxed to their minima at each value of  $\theta$ . The ridge line is shown with a solid black line, and the locations of TS2 and TS2' are indicated.

The configuration of TS2 is first found using a standard saddle point search in the  $3n$ -dimensional full configuration space using CASPT2/aug-cc-pVTZ (6o, 6e) with the Molpro package. The lowest nonzero frequency mode is found to correspond to mostly displacement in the dihedral angle. Therefore, we carry out a set of constrained saddle point searches where the dihedral angle is held fixed. The value of the dihedral angle is scanned over  $2\pi$  starting at TS2. In this way the ridge line  $\mathbf{R}(\theta)$  is mapped out. To characterize the properties of the saddle points obtained for each of the constrained structures, a normal-mode analysis was carried out at each value of  $\mathbf{R}(\theta)$ . In this analysis, the frequencies were obtained by diagonalizing the projected force constant matrix

$$\mathbf{F}_{\text{proj}} = \mathbf{P}\mathbf{F}\mathbf{P}^{-1} \quad (4.2)$$

Here,  $\mathbf{F}$  is the conventional Hessian matrix in the mass-weighted Cartesian coordinates of the full configuration space and  $\mathbf{P}$  is a projection operator. We compose  $\mathbf{P}$  as a product of one-dimensional projectors that locally eliminate the subspaces for translation, overall rotation, and torsion. Diagonalizing the matrix  $\mathbf{F}_{\text{proj}}$  yields the instantaneous normal modes of the transition state complex as a function of  $\theta$ . There are  $3n - 8$  real frequencies,  $\omega(\theta) = (\omega_1(\theta), \dots, \omega_{3n-8}(\theta))$ , and one imaginary frequency  $i\omega_s(\theta)$  associated with the local reaction coordinate  $s$ . Here,  $n$  is the number of atoms so there are  $3n - 8 = 10$  normal modes excluding torsion and the reaction coordinate. In Figure 5, we show the 10 instantaneous normal-mode frequencies for the  $\text{HO}_2 + \text{HO}_2$  transition state ridge as a function of the dihedral angle. The nonseparability of the torsional motion is apparent from the large variation of the frequencies. Of course, since the torsional displacement gives rise to large geometric changes in the adduct, the principle moments of inertia are also functions of  $\theta$ . We should point out that while the torsional mode we have defined is not precisely a normal mode, the frequencies from the full normal-mode analysis and the constrained normal-mode analysis at TS2 and TS2' are nearly the same.

The framework of our treatment is based on the observation that the torsion is the slowest vibrational mode at the transition state. Therefore, we adopt a vibrationally adiabatic approach in which the energy levels for the remaining "fast" vibrational degrees of freedom instantaneously adjust to the "slow"

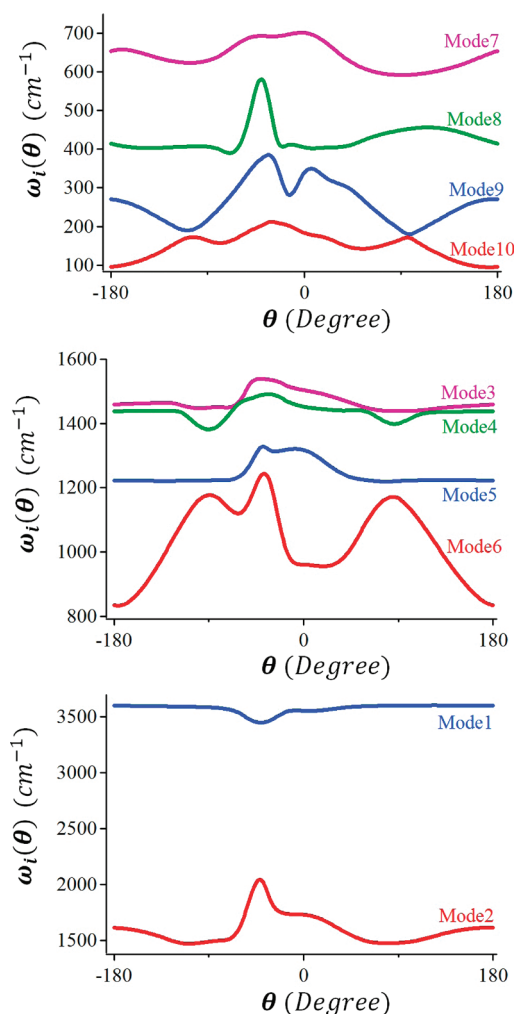


**Figure 5.** Frequencies of the 10 normal modes of the  $\text{H}_2\text{O}_4$  transition state complex (excluding the reaction coordinate and the torsion) as a function of the dihedral angle of the torsion. The strong mode coupling seen here is especially important for the low frequency modes.

torsional motion. Hence, the vibrational energy levels of the  $3n - 8$  dimensional constrained complex are

$$\epsilon_{\mathbf{n}}(\theta) = \sum_{i=1}^{3n-8} \hbar \omega_i(\theta) [n_i + 1/2] \quad (4.3)$$

where the quantum numbers,  $\mathbf{n}$ , are conserved during torsional motion. The full vibrational energy,  $\epsilon_{\mathbf{n},k}$  of a given state is then obtained by solving the vibrationally adiabatic Schrodinger equation for the torsion degree of freedom, i.e.

$$\left[ \frac{\hat{p}_\theta^2}{2I_\theta} + \epsilon_{\mathbf{n}}(\theta) + V(\theta) \right] \varphi_k(\theta) = \epsilon_{\mathbf{n},k} \varphi_k(\theta) \quad (4.4)$$

where  $(\mathbf{n}, k)$  form a complete set of  $3n - 7$  vibrational quantum numbers for the transition state and  $V(\theta)$  is the Born–Oppenheimer potential along the ridge line. The torsional moment of inertia is given by<sup>58</sup>

$$I_\theta = \frac{I_1 I_2}{I_1 + I_2} \quad (4.5)$$

with

$$I_1 = m_{\text{O}} \cdot (d_{\text{O}1})^2 \quad (4.6)$$

$$I_2 = m_{\text{O}} \cdot (d_{\text{O}4})^2 + m_{\text{H}} \cdot (d_{\text{H}6})^2 \quad (4.7)$$

Here,  $m_{\text{O}}$  and  $m_{\text{H}}$  are the masses of oxygen and hydrogen atoms, and  $d_{\text{O}1}$ ,  $d_{\text{O}4}$ , and  $d_{\text{H}6}$  are the vertical distance to the  $\text{O}_2\text{--O}_3$  torsional axis of atoms 1, 4, and 6. We can define adiabatic rotational levels since the principle moments of inertia are also functions of  $\theta$

$$\epsilon_{jk}^{\text{rot}}(\theta) = \frac{\hbar^2}{2I_1} j(j+1) + \frac{\hbar^2 k^2}{2I_3} \left( \frac{1}{2I_3} - \frac{1}{2I_1} \right) \quad (4.8)$$

The rotations are not slow compared to the torsional motion, but the errors incurred using this approximation are small in the final expressions.

If we numerically solve the one-dimensional Schrodinger eq 4.4 for every physically relevant 10-tuple of quantum numbers,  $n$ , the vibrational energy levels may be explicitly generated and the cumulative state density may be directly computed. Since this may require 100 000s of solutions to eq 4.4, we instead adopt a simpler semiclassical approach. We know the quantum expression for the cumulative vibration state density is

$$N_{\text{Q}}(E) = \text{Tr} \Theta(E - \hat{H}) \quad (4.9)$$

where  $\Theta$  is the Heaviside step-function and  $\hat{H}$  is the  $3n - 7$  dimensional vibrational Hamiltonian. Analogously, the semiclassical expression makes use of phase space integration

$$N_{\text{sc}}(E) = \frac{1}{h^{3n-7}} \int \Theta(E - H) \prod_{i=1}^{3n-7} dp_i dq_i \quad (4.10)$$

where  $H$  is the classical analogue of  $\hat{H}$ . We adopt a mixed representation where the torsion is treated classically and the remaining coordinates are treated quantum mechanically. Thus we have

$$N_{\text{mixed}}(E) = \frac{1}{h} \int [\text{Tr}' \Theta(E - H_{\text{mixed}})] dp_{\theta} d\theta \quad (4.11)$$

where the  $H_{\text{mixed}}$  has classical torsion but quantum normal mode vibration, i.e.

$$H_{\text{mixed}} = \frac{p_{\theta}^2}{2I_{\theta}} + V(\theta) + \sum_{i=1}^{3n-8} \frac{\widehat{p}_i^2 + \omega_i^2(\theta) \widehat{q}_i^2}{2} \quad (4.12)$$

The partial trace,  $\text{Tr}'$ , is taken over the quantum variables only. To evaluate eq 4.11 we first carry out the partial trace at fixed values of  $(p_{\theta}, \theta)$ . This yields

$$N_{\text{mixed}}(E) = \frac{1}{h} \int \tilde{N} \left( E - \frac{p_{\theta}^2}{2I_{\theta}}, \theta \right) dp_{\theta} d\theta \quad (4.13)$$

where

$$\tilde{N}(E', \theta) = \text{Tr}' \Theta \left( E' - \sum_{i=1}^{3n-8} \frac{\widehat{p}_i^2 + \omega_i^2(\theta) \widehat{q}_i^2}{2} \right) \quad (4.14)$$

and the energy is shifted as  $E' = E - (p_{\theta}^2/(2I_{\theta})) - V(\theta)$ . Thus  $\tilde{N}(E', \theta)$  is the usual cumulative state density for the  $3n - 8$  normal modes at fixed  $\theta$ . We evaluate eq 4.13 using numerical

quadrature by first constructing a two-dimensional table of  $\tilde{N}(E', \theta)$  for the relevant range of energies and angles, which are then used to create an efficient tensor spline representation of the function. An illustration of the variation of  $\tilde{N}$  with dihedral angle is shown in Figure 6. For the case of  $E' = 5000 \text{ cm}^{-1}$ , it is

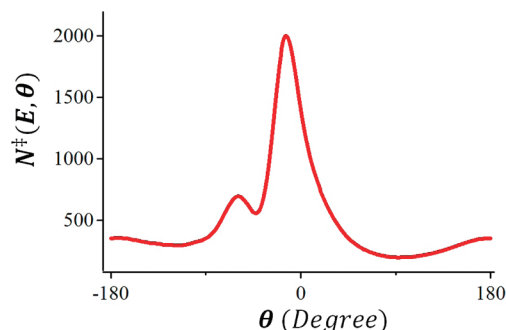


**Figure 6.** Cumulative state density at the inner transition state as a function of the dihedral angle. The calculation was carried out for  $E = 5000 \text{ cm}^{-1}$  above the entrance channel zero point and includes vibration only. Under these conditions, state density near TS2 dominates over TS2'.

seen that the cumulative state density near TS2 ( $\theta = -25.5^\circ$ ) dominates over that of TS2' ( $\theta = -167.6^\circ$ ).

It is known that the semiclassical expression, eq 4.10, suffers error if the effects of zero-point energy are not included. In our mixed representation the zero point of all  $3n - 8$  nontorsional normal modes is fully included within  $\tilde{N}_{\text{mixed}}(E', \theta)$ , so that only the torsional zero point is neglected in  $N_{\text{mixed}}$ . Thus, to improve the result at the level of the Marcus–Rice approximation<sup>59</sup> the torsional zero point computed at TS2 ( $\epsilon_0 = 59.8 \text{ cm}^{-1}$ ) is added to the energy argument of eq 4.14.

Finally, to obtain the total cumulative density of state including the rotational contributions, it is necessary to sum over the rotational progressions along the transition state ridge. Complicating the analysis slightly is the  $\theta$  dependence of the rotational constants. Using the adiabatic model we write in analogy to eq 4.1

$$\begin{aligned} N_{\text{mixed}}(E, J) = & \frac{1}{h} \int \tilde{N} \left( E - \epsilon_0 - \frac{p_{\theta}^2}{2I_{\theta}} - \frac{\hbar^2 J(J+1)}{2I_1(\theta)}, \theta \right) \\ & \times dp_{\theta} d\theta + \sum_{k=1}^J 2 \cdot \frac{1}{h} \\ & \times \int \tilde{N} \left( E - \epsilon_0 - \frac{p_{\theta}^2}{2I_{\theta}} - \frac{\hbar^2 J(J+1)}{2I_1(\theta)} \right. \\ & \left. - \hbar^2 k^2 \left( \frac{1}{2I_3(\theta)} - \frac{1}{2I_1(\theta)} \right), \theta \right) dp_{\theta} d\theta \end{aligned} \quad (4.15)$$

This gives the cumulative density of states at the inner transition state up to the  $(2J + 1)$  overall rotational degeneracy factor. It should be noted that eq 4.15 is no more complicated to evaluate than the vibration only expression, eq 4.13, since the rotational terms are merely an energy shift that can be accounted for using the same tensor spline representation of  $\tilde{N}(E', \theta)$  used above.



## V. QUANTUM TUNNELING

The imaginary frequency along the transition state ridge is found to be quite high (see Figure 7). It is expected, therefore,

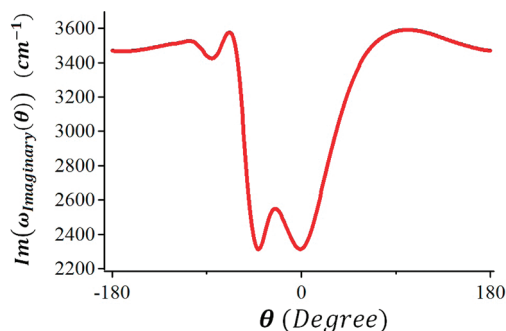


**Figure 7.** Imaginary frequency of the transition state ridge as a function of the dihedral angle.

that quantum tunneling should play a significant role in the reaction. Since most treatments of tunneling are referenced to a single saddle point, it is not initially obvious how to include tunneling through the ridge, which can be thought of as a one parameter family of saddle points. Therefore, we shall propose here a very simple scheme to incorporate tunneling through the transition state ridge.

The generally accepted procedure to include tunneling in a RRKM determination of the rate is to replace the classical (i.e., no tunneling) cumulative density of states  $N(E)$  with

$$N_q(E) = \int_{E_{TS}}^{\infty} \rho(\epsilon) \cdot P(E - \epsilon) \cdot d\epsilon \quad (5.1)$$

where the state density is  $\rho(\epsilon) = dN(\epsilon)/d\epsilon$  and  $P(E - \epsilon)$  is the quantum transmission probability at the translational energy  $E - \epsilon$ . The energy  $\epsilon$  is the total excitation energy of the  $3n - 8$  transition state modes. For ridge tunneling in the adiabatic approximation, we can assume that the tunneling dynamics occurs at fixed  $\theta$ ; i.e., the torsion is dynamically frozen. Thus, a tunneling probability at each  $\theta$  value,  $P(E - \epsilon, \theta)$ , may be determined by applying the tunneling method of choice to the torsionally constrained Hamiltonian,  $H(\theta = \text{constant})$ . We can calculate the quantum transmission probability at fixed  $\theta$  by simply applying eq 5.1 separately to each  $\theta$  value. Thus, in place of the classical  $\tilde{N}(E, \theta)$  we have the quantum expression

$$\tilde{N}_q(E', \theta) = \int_{E_{TS}(\theta)}^{\infty} \tilde{\rho}(\epsilon, \theta) \cdot P(E - \epsilon, \theta) \cdot d\epsilon \quad (5.2)$$

where  $\tilde{\rho}(E, \theta) = d\tilde{N}(E, \theta)/dE$ . The use of this expression in place of eq 4.14 then provides one method to incorporate tunneling in the present problem.

We have chosen to model the tunneling using the small curvature tunneling (SCT) method which has proven to be an effective approach in numerous previous studies.<sup>60,61</sup> This method takes into account the corner cutting tendency of the tunneling for problems with a curved minimum energy path (MEP) near the TS. Since the recalculation of the MEP at many values of  $\theta$  proved to be a laborious chore, we adopted the following streamlined procedure. The reaction path and the SCT transmission function  $P(E, \theta)$  were computed at the  $\theta$  values corresponding to TS2 and TS2'. We then interpolate  $P(E, \theta)$  to other values of  $\theta$  using a parabolic tunneling formula. Thus, the tunneling through TS2 and TS2' is "exact", and the

values between are interpolated based on the imaginary frequency and height of the effective barrier.

## VI. RESULTS AND DISCUSSION

Using the formalism described above, we have computed the canonical rate coefficient over the temperature range of 200–2000 K and pressure range 0–10 atm. To obtain agreement with experiment, we have found it necessary to shift the energy of the transition state ridge upward by 1 kcal/mol. This is within our error estimates for the quantum chemistry. In Figure 8,

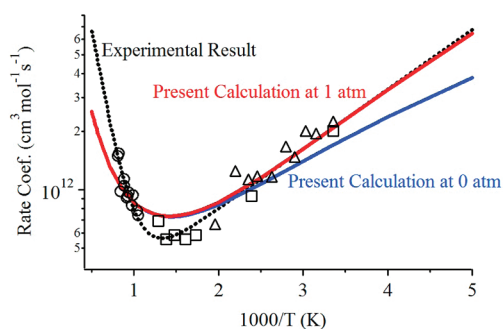


**Figure 8.**  $\text{HO}_2 + \text{HO}_2$  rate coefficient versus temperature. The red curve is the present calculation at  $p = 1$  atm, and the blue curve is for  $p = 0$ . The experimental results  $\Delta$  (ref 7),  $\square$  (ref 14), and  $\circ$  (ref 21) are shown for reference. The dashed black curve is a fitting of the experimental results consistent with  $p = 1$  atm of  $\text{N}_2$ .

we show the results of our theory for  $p = 0$  and 1 atm. Using a nonlinear least-squares procedure we have fit our numerical results to a two exponential expression (in  $\text{cm}^3 \text{mol}^{-1} \text{s}^{-1}$ )

$$k_{\text{theory}}(p = 1 \text{ atm}) = 1.179 \times 10^9 \cdot T^{0.7712} \cdot \exp\left(\frac{918.19}{T}\right) + 1.251 \times 10^{12} \cdot T^{0.2950} \cdot \exp\left(\frac{-3724.7}{T}\right) \quad (6.1)$$

$k_{\text{theory}}(p = 0)$  and  $k_{\text{theory}}(p = 1 \text{ atm})$  differ by roughly a factor of 1.4 at low  $T$  while becoming virtually identical for  $T > 500 \text{ K}$ . For comparison, we also plot a fitting of various low and high temperature experimental results that was constructed by Troe and co-workers,<sup>21</sup> i.e.

$$k_{\text{exp}}(\text{cm}^3 \text{mol}^{-1} \text{s}^{-1}) = 1.03 \times 10^{14} \cdot \exp(-5556 \text{ K}/T) + 1.94 \times 10^{11} \cdot \exp(709 \text{ K}/T) \quad (6.2)$$

The experimental low temperature results<sup>7,14,15</sup> used in this fit were gathered at total pressures near 1 atm in an environment consisting of mostly  $\text{N}_2$  buffer gas. It is seen that the theoretical rate coefficient gives a U-shaped curve versus  $1/T$ , with negative activation energy at low- $T$  and positive activation energy at high  $T$ . The shape of the function and location of the minimum near  $T = 800 \text{ K}$  is consistent with experiment. At low temperatures, the theory and experiment agree quite well. For temperatures less than 500 K, the theoretical rate coefficient is no more than 25% higher than the three sets of experimental results of Pilling,<sup>5</sup> Lesclaux,<sup>14</sup> Jenkins,<sup>15</sup> and their co-workers. The high  $T$  predictions are also in reasonable agreement with experiment showing an increasing rate coefficient above 1000 K. Unlike the low  $T$  result, the high  $T$   $k_{\text{obs}}(T)$  is largely insensitive to pressure effects. Hence, it is gratifying that the reasonable agreement with experiment is achieved independently

of empirically adjusted collisional parameters. We do note, however, that our theoretical  $k_{\text{obs}}(T)$  grows less rapidly versus  $T$  than does the shock tube experiments of Troe and workers.<sup>16,21</sup> At 1250 K (the highest temperature reported), the experiment is roughly a factor of 1.5 larger than theory. If the extrapolation of eq 6.2 to higher temperatures is valid, then the differences between theory and experiment grow larger with  $T$ , becoming nearly a factor of 3 by  $T = 2000$  K. These differences may lead to important consequences in future modeling work.

It is worthwhile to point out that the same shock tube studies of  $\text{H}_2\text{O}_2$  pyrolysis conducted by Troe and co-workers<sup>16,21</sup> which led to the  $\text{HO}_2 + \text{HO}_2$  rate coefficient, also produced rate coefficients for the processes  $\text{OH} + \text{H}_2\text{O}_2 \rightarrow \text{HO}_2 + \text{H}_2\text{O}$  and  $\text{OH} + \text{HO}_2 \rightarrow \text{H}_2\text{O} + \text{O}_2$ . The  $k(T)$  for these processes showed rapid increase at high temperature, analogous to the  $\text{HO}_2$  self-reaction. Recently, Hanson and co-workers<sup>62,63</sup> have performed new experiments at even higher temperatures that showed somewhat different behavior for the  $\text{OH} + \text{H}_2\text{O}_2$  and  $\text{OH} + \text{HO}_2$  reactions. In particular, Hanson and co-workers found a flattening out of the  $\text{OH} + \text{HO}_2$  rate coefficient at temperature between 1600 and 2200 K. These results did not appear to follow a smooth extrapolation of the lower temperature results of Troe and co-workers. The  $\text{OH} + \text{H}_2\text{O}_2$  was found to be substantially lower and more slowly increasing than that of Troe et al., although this was a less direct measurement. There was broad agreement for the rate of  $\text{H}_2\text{O}_2$  dissociation. To assess the high temperature behavior of  $\text{HO}_2 + \text{HO}_2$ , and the possibility of a similar high temperature flattening, it would be interesting to have additional experimental results.

The two main theoretical innovations of the present work are the vibrationally adiabatic modeling of the torsion and the associated inclusion of the tunneling through the transition state ridge. To assess the importance of this methodology, we carried out several additional calculations using alternate methods. First, we have calculated the rate coefficient using the standard normal-mode treatment of the torsion. We have carried out a determination of the rate coefficient assuming, in turn,  $N_2^\ddagger(E, J) = N_{\text{TS2}}^\ddagger(E, J)$ ,  $N_2^\ddagger(E, J) = N_{\text{TS2}'}^\ddagger(E, J)$ , and  $N_2^\ddagger(E, J) = N_{\text{TS2}}^\ddagger(E, J) + N_{\text{TS2}'}^\ddagger(E, J)$  in eq 2.4. Tunneling was included using the conventional SCT method. As seen in Figure 9, the

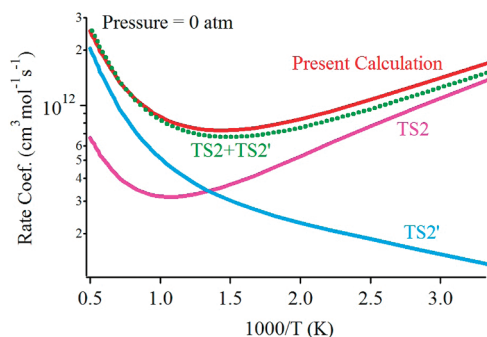


**Figure 9.** Theoretical rate coefficient calculated using several methods. The red line is the full calculation with the vibrationally adiabatic treatment of the torsion. The TS2 and TS2' curves are the results using the normal-mode treatment of the two saddle points. The TS2 + TS2' curve is the result of summing the flux through both transition states. All calculations include tunneling.

lower transition state, TS2, dominates over TS2' at low  $T$ . However, at high  $T$  the higher transition state TS2' dominates. Computing  $k_{\text{obs}}(T)$  using the sum  $N_{\text{TS2}}^\ddagger(E, J) + N_{\text{TS2}'}^\ddagger(E, J)$  is analogous to the simple MS-AS-HO method of Truhlar and

co-workers.<sup>57</sup> Interestingly, this approach gives a result quite close to the more sophisticated adiabatic model. It is likely that the agreement between these approaches is fortuitous. Indeed, at lower levels of QM the shallow TS2' saddle point actually disappears. In this case, the appropriate calculation would be  $N_2^\ddagger(E, J) = N_{\text{TS2}}^\ddagger(E, J)$ , which is clearly inadequate as seen in Figure 9.

Another conventional approach is to model the torsional motion using a separable hindered rotor while computing the remaining normal-mode frequencies at the conventional transition state. When the hindered rotor approximation is made at the TS2 saddle point, we refer to the resulting rate as  $\overline{\text{TS2}}$ . In Figure 10 we plot the results for the hindered rotor model

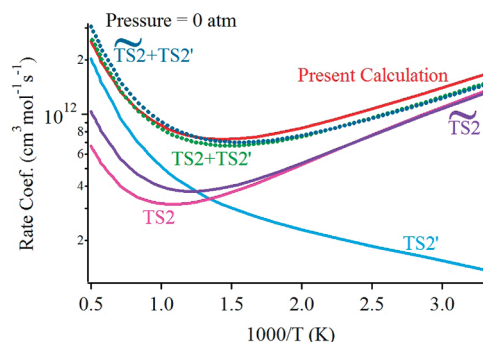


**Figure 10.** Several additional methods for computing the rate coefficient. The rate coefficient computed using a hindered rotor model at the TS2 saddle point is denoted by  $\overline{\text{TS2}}$ . The remaining rate expressions are identical to those shown in Figure 9.

along with the previously obtained results. It is seen that at low  $T$ , the hindered rotor model is essentially equivalent to the standard normal-mode treatment. At high  $T$ , the result is somewhat higher than the TS2 normal-mode analysis, but is still far too low compared to either experiment or the adiabatic torsion model. The sum expression  $\overline{\text{TS2}} + \text{TS2}'$  appears to be roughly comparable to the normal mode TS2 + TS2'.

We have also carried out calculations in which tunneling through the inner transition state is ignored, but where we have retained the vibrationally adiabatic treatment of the torsion. As seen in Figure 11, the value of  $k_{\text{obs}}(T)$  is significantly reduced at

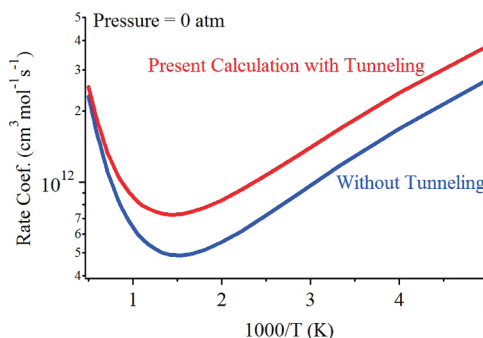


**Figure 11.** Low pressure rate coefficient calculated with and without the SCT tunneling correction.

low temperatures. Below 400 K, the tunneling contributed almost a factor of 2 to the rate coefficient. It is gratifying to note that the experimental results are more consistent with the results that include tunneling. At high temperatures, above 1000 K, the influence of tunneling steadily wanes.

Finally, it is interesting to consider the role of third body collisions. Kircher and Sander<sup>10</sup> noted a pronounced pressure enhancement at ambient temperatures and pressures. This enhancement became weaker as the temperature increased and presumably disappears above  $T = 500$  K. This is likely due to the collisional stabilization of the  $\text{H}_2\text{O}_4$  complex and suppression of the back reaction  $\text{H}_2\text{O}_4 \rightarrow 2\text{HO}_2$ . Using the master equation formalism, we have estimated the enhancement factor over a range of temperatures and pressures. In Figure 12 we show  $k_{\text{obs}}(T, p)/k_{\text{obs}}(T, p = 0)$  for  $p \in (0, 10 \text{ atm})$

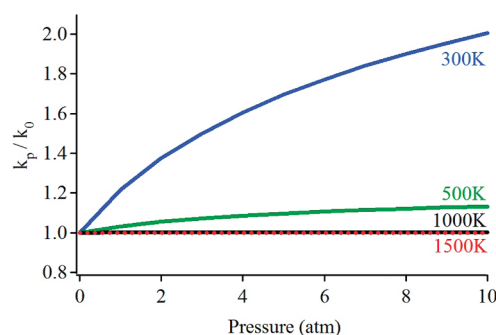


**Figure 12.** Enhancement of the computed rate coefficient,  $k_{\text{obs}}(T, p)/k_{\text{obs}}(T, p = 0)$  as a function of pressure for several temperatures.

and  $T = 300, 500, 1000$ , and  $1500$  K. It is seen that the enhancement at  $p = 1$  atm is negligible at  $T = 500$  K and is negligible at all pressures below  $10$  atm above  $700$  K. The enhancements predicted by the theory are qualitatively similar to those observed experimentally by Kircher and Sander although there are quantitative differences.

## ■ ASSOCIATED CONTENT

### ■ Supporting Information

Cartesian coordinates, energies, and normal-mode frequencies. This material is available free of charge via the Internet at <http://pubs.acs.org>.

## ■ AUTHOR INFORMATION

### Corresponding Author

\*E-mail: [rex.skodje@colorado.edu](mailto:rex.skodje@colorado.edu).

### Notes

The authors declare no competing financial interest.

## ■ ACKNOWLEDGMENTS

This work was supported by the Division of Chemical Sciences, Geosciences, and Biosciences, the Office of Basic Energy Sciences, the U.S. Department of Energy, under contract number DE-AC02-06CH11357. We are also grateful to the Chinese Academy of Sciences for support through the program for visiting professorships for senior international scientists. We thank Yuri Georgievskii for assistance with the VariFlex program.

## ■ REFERENCES

- (1) Troe, J. *Ber. Bunsen-Ges. Phys. Chem.* **1969**, *73*, 906–907.
- (2) Hochanadel, C. J.; Ghormley, J. A.; Ogren, P. J. *J. Chem. Phys.* **1972**, *56*, 4426–4432.
- (3) Paukert, T. T.; Johnston, H. S. *J. Chem. Phys.* **1972**, *56*, 2824–2838.
- (4) Hamilton, E. J. *J. Chem. Phys.* **1975**, *63*, 3682–3683.
- (5) Hamilton, E. J.; Lii, R. R. *Int. J. Chem. Kinet.* **1977**, *9*, 875–885.

- (6) Cox, R. A.; Burrows, J. P. *J. Phys. Chem.* **1979**, *83*, 2560–2568.
- (7) Patrick, R.; Pilling, M. J. *Chem. Phys. Lett.* **1982**, *91*, 343–347.
- (8) Thrush, B. A.; Tyndall, G. S. *J. Chem. Soc., Faraday Trans. 2* **1982**, *78*, 1469–1475.
- (9) Patrick, R.; Barker, J. R.; Golden, D. M. *J. Phys. Chem.* **1984**, *88*, 128–136.
- (10) Kircher, C. C.; Sander, S. P. *J. Phys. Chem.* **1984**, *88*, 2082–2091.
- (11) Glinski, R. J.; Birks, J. W. *J. Phys. Chem.* **1985**, *89*, 3449–3453.
- (12) Mozurkewich, M.; Benson, S. W. *Int. J. Chem. Kinet.* **1985**, *17*, 787–807.
- (13) Sahetchian, K. A.; Heiss, A.; Rigny, R. *J. Phys. Chem.* **1987**, *91*, 2382–2386.
- (14) Lightfoot, P. D.; Veyret, B.; Lesclaux, R. *Chem. Phys. Lett.* **1988**, *150*, 120–126.
- (15) Andersson, B. Y.; Cox, R. A.; Jenkins, M. E. *Int. J. Chem. Kinet.* **1988**, *20*, 283–295.
- (16) Hippler, H.; Troe, J.; Willner, J. *J. Chem. Phys.* **1990**, *93*, 1755–1760.
- (17) Maricq, M. M.; Szente, J. L. *J. Phys. Chem.* **1994**, *98*, 2078–2082.
- (18) Hippler, H.; Neunaber, H.; Troe, J. *J. Chem. Phys.* **1995**, *103*, 3510–3516.
- (19) Zhu, R.; Lin, M. C. *PhysChemComm* **2001**, *23*, 1–1.
- (20) Zhu, R.; Lin, M. C. *Chem. Phys. Lett.* **2002**, *354*, 217–226.
- (21) Kappel, C.; Luther, K.; Troe, J. *Phys. Chem. Chem. Phys.* **2002**, *4*, 4392–4398.
- (22) Donaldson, D. J.; Francisco, J. S. *Phys. Chem. Chem. Phys.* **2003**, *5*, 3183–3187.
- (23) Atkinson, R.; Baulch, D. L.; Cox, R. A.; Crowley, J. N.; Hampson, R. F.; Hynes, R. G.; Jenkin, M. E.; Rossi, M. J.; Troe, J. *Atmos. Chem. Phys.* **2004**, *4*, 1461–1738.
- (24) Stone, D.; Rowley, D. M. *Phys. Chem. Chem. Phys.* **2005**, *7*, 2156–2163.
- (25) Kanno, N.; Tonokura, K.; Tezaki, A.; Koshi, M. *J. Phys. Chem. A* **2005**, *109*, 3153–3158.
- (26) Baulch, D. L.; Bowman, C. T.; Cobos, C. J.; Cox, R. A.; Just, T.; Kerr, J. A.; Pilling, M. J.; Stocker, D.; Troe, J.; Tsang, W.; Walker, R. W.; Warnatz, J. *J. Phys. Chem. Ref. Data* **2005**, *34*, 757–1397.
- (27) Anglada, J. M.; Olivella, S.; Sole, A. *J. Phys. Chem. A* **2007**, *111*, 1695–1704.
- (28) Tang, Y.; Tyndall, G. S.; Orlando, J. J. *J. Phys. Chem. A* **2010**, *114*, 369–378.
- (29) Tyndall, G. S.; Cox, R. A.; Granier, C.; Lesclaux, R.; Moortgat, G. K.; Pilling, M. J.; Ravishankara, A. R.; Wallington, T. J. *J. Geophys. Res., [Atmos.]* **2001**, *106*, 12157–12182.
- (30) Sahetchian, K. A.; Heiss, A.; Rigny, R. *J. Phys. Chem.* **1987**, *91*, 2382–2386.
- (31) Skodje, R. T.; Tomlin, A. S.; Klippenstein, S. J.; Harding, L. B.; Davis, M. J. *J. Phys. Chem. A* **2010**, *114*, 8286–8301.
- (32) Klippenstein, S. J.; Harding, L. B.; Davis, M. J.; Tomlin, A. S.; Skodje, R. T. *Proc. Combust. Inst.* **2011**, *33*, 351–357.
- (33) Davis, M. J.; Skodje, R. T.; Tomlin, A. S. *J. Phys. Chem. A* **2011**, *115*, 1556–1578.
- (34) Westbrook, C. K. *Proc. Combust. Inst.* **2000**, *28*, 1563–1577.
- (35) Troe, J. *J. Chem. Soc., Faraday Trans.* **1994**, *90*, 2303–2317.
- (36) Troe, J.; Ushakov, V. G. *J. Phys. Chem. A* **2006**, *110*, 6732–6741.
- (37) Giguere, P. A.; Herman, K. *Can. J. Chem.* **1970**, *48*, 3473–3480.
- (38) Howard, C. J. *Proc. NATO Adv. Study Inst. Atmos. Ozone* **1979**, 409–427.
- (39) Lii, R. R.; Gorse, R. A.; Sauer, M. C.; Gordon, S. J. *Phys. Chem.* **1979**, *83*, 1803–1804.
- (40) Mozurkewich, M.; Benson, S. W. *J. Phys. Chem.* **1984**, *88*, 6429–6435.
- (41) Chen, Y.; Rauk, A.; Tschuikow-Roux, E. *J. Phys. Chem.* **1991**, *95*, 9900–9908.
- (42) Georgievskii, Y.; Klippenstein, S. J. *J. Phys. Chem. A* **2007**, *111*, 3802–3811.

- (43) Holbrook, K. A.; Pilling, M. J.; Robertson, S. T. *Unimolecular Reactions*, 2nd ed.; John Wiley and Sons: New York, 1996.
- (44) Barker, J. R. *Chem. Phys.* **1983**, *77*, 301–318.
- (45) Fitzgerald, G.; Schaefer, H. F. *J. Chem. Phys.* **1984**, *81*, 362–367.
- (46) Fitzgerald, G.; Lee, T. J.; Bartlett, R. J.; Schaefer, H. F. *J. Chem. Phys.* **1985**, *83*, 6275–6282.
- (47) Werner, H. J. *Mol. Phys.* **1996**, *89*, 645–661. Celani, P.; Werner, H. J. *J. Chem. Phys.* **2000**, *112*, 5546–5557.
- (48) Werner, H. J.; Knowles, P. J.; Lindh, R.; Manby, F. R.; Schütz, M.; Celani, P.; Korona, T.; Mitrushenkov, A.; Rauhut, G.; Adler, T. B.; Amos, R. D.; Bernhardsson, A.; Berning, A.; Cooper, D. L.; Deegan, M. J. O.; Dobbyn, A. J.; Eckert, F.; Goll, E.; Hampel, C.; Hetzer, G.; Hrenar, T.; Knizia, G.; Köppl, C.; Liu, Y.; Lloyd, A. W.; Mata, R. A.; May, A. J.; McNicholas, S. J.; Meyer, W.; Mura, M. E.; Nicklass, A.; Palmieri, P.; Pflüger, K.; Pitzer, R.; Reiher, M.; Schumann, U.; Stoll, H.; Stone, A. J.; Tarroni, R.; Thorsteinsson, T.; Wang, M.; Wolf, A. MOLPRO, version 2010.1, a package of ab initio programs (<http://www.molpro.net>).
- (49) Martin, J. M. L.; Uzan, O. *Chem. Phys. Lett.* **1998**, *282*, 16–24.
- (50) Knowles, P. J.; Hampel, C.; Werner, H. J. *J. Chem. Phys.* **1993**, *99*, 5219–5227. Erratum. *J. Chem. Phys.* **2000**, *112*, 31063107.
- (51) Zheng, J. et al. POLYRATE: Computer Program for the Calculation of Chemical Rates for Polyatomics, version 2010-A; University of Minnesota: Minneapolis, MN, 2010.
- (52) Klippenstein, S. J.; Wagner, A. F.; Robertson, S. H.; Dunbar, R. C.; Wardlaw, D. M. VariFlex, version 1999 (<http://chemistry.anl.gov/chen-dyn/VariFlex>).
- (53) Georgievskii, Y.; Klippenstein, S. J. *J. Chem. Phys.* **2003**, *118*, 5442–5455.
- (54) Beyer, T.; Swinehart, D. F. *Commun. ACM* **1973**, *16*, 379–379.
- (55) Sharma, S.; Raman, S.; Green, W. H. *J. Phys. Chem. A* **2010**, *114*, 5689–5701.
- (56) Vansteenkiste, P.; Van Neck, D.; Van Speybroeck, V.; Waroquier, M. *J. Chem. Phys.* **2006**, *124*, 044314–044314.
- (57) Zheng, J.; Yu, T.; Papajak, E.; Alecue, I. M.; Mielke, S. L.; Truhlar, D. G. *Phys. Chem. Chem. Phys.* **2011**, *13*, 10885–10907.
- (58) Chuang, Y. Y.; Truhlar, D. G. *J. Chem. Phys.* **2000**, *112*, 1221–1228.
- (59) Marcus, R. A.; Rice, O. K. *J. Phys. Colloid. Chem.* **1951**, *55*, 894–908.
- (60) Skodje, R. T.; Truhlar, D. G.; Garrett, B. C. *J. Phys. Chem.* **1981**, *85*, 3019–3023.
- (61) Liu, Y. P.; Lynch, G. C.; Truong, T. N.; Lu, D. H.; Truhlar, D. G. *J. Am. Chem. Soc.* **1993**, *115*, 2408–2415.
- (62) Hong, Z.; Cook, R. D.; Davidson, D. F.; Hanson, R. K. *J. Phys. Chem. A* **2010**, *114*, 5718–5727.
- (63) Hong, Z.; Vasu, S. S.; Davidson, D. F.; Hanson, R. K. *J. Phys. Chem. A* **2010**, *114*, 5520–5525.